ACS APPLIED BIO MATERIALS

www.acsabm.org Article

Enabling High-Performance Surfaces of Biodegradable Magnesium Alloys via Femtosecond Laser Shock Peening with Ultralow Pulse Energy

Wenbo Wang, Chang-Yu Hung, Leslie Howe, Jia Chen, Kaiwen Wang, Vinh X. Ho, Shannon Lenahan, Mitsuhiro Murayama, Nguyen Q. Vinh,* and Wenjun Cai*

Cite This: *ACS Appl. Bio Mater.* 2021, 4, 7903−7912 Read Online

ACCESS | Metrics & More | Article Recommendations | Supporting Information

ABSTRACT: The fast degradation rate and poor wear resistance of magnesium (Mg) alloys in physiological environments have limited their potential usage as next-generation biodegradable orthopedic implant materials. In this work, femtosecond laser shock peening (fs-LSP) was successfully applied to simultaneously improve the surface mechanical, corrosion, and tribocorrosion properties of WE43 Mg alloys in blood bank buffered saline solution at body temperature. Specifically, the treated surfaces of WE43 Mg alloys via fs-LSP with ultralow pulse energy were investigated under different power densities, confining mediums, and absorbent materials. It was found that the combination of a black tape and a quartz layer gave the optimum peening effect under a power density of 28 GW/cm^2, which simultaneously strengthened the surface and reduced the corrosion kinetics. In addition, a rapid self-repassivation was observed in fs-LSP-treated WE43 surfaces during tribocorrosion, promising sustained corrosion resistance under mechanical loading, critical to the reliability of load-bearing implants. Finally, the subsurface microstructural evolution and residual stress development in WE43 after fs-LSP were discussed based on the results from transmission electron microscopy analysis and finite element simulations.

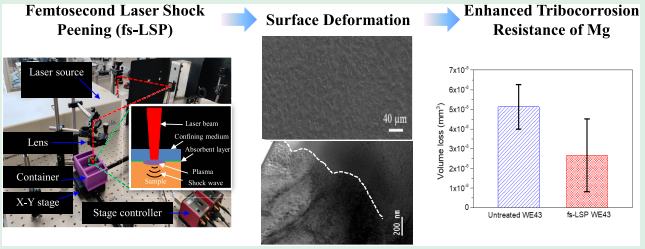

KEYWORDS: *femtosecond laser shock peening, biodegradable metal, magnesium, corrosion, tribocorrosion, compressive residual stress*

1. INTRODUCTION

Strong and corrosion-resistant metallic materials such as stainless steel, cobalt-, and titanium-based alloys have been successfully applied as permanent orthopedic implant materials owing to their reliable structural stability in physiological conditions.[1,2] However, these materials often exhibit a high mismatch in stiffness and elastic modulus as compared to natural bone, causing stress shielding complications that ultimately reduce the density of the surrounding bone and weaken the bone structure.[3−5] In addition, the high corrosion resistance indicates that they would remain in vivo permanently if no follow-up removal operation was performed, which could lead to enduring physical irritation or inflammatory discomfort.[6,7] Recently, biodegradable alloys have attracted significant interest in the orthopedic industry due to their suitable mechanical properties and high degradation rate, potentially eliminating both the stress fielding problem as well as the secondary removal surgery.[8] Specifically, magnesium (Mg) and its alloys stand out among various degradable metals,[9,10] exhibiting outstanding biocompatibility with similar mechanical properties as human bone (i.e., E_{bone} = 3−20 GPa; E_{Mg} = 41−45 GPa), and excellent implant stability. In addition, Mg also serves as a nutritional element that is essential to human metabolism to facilitate bone tissue growth.[11]

Unfortunately, the rapid degradation rate of Mg alloys in the physiological environment under a pH of ∼7.4−7.6 makes it challenging to ensure adequate structural integrity over the required time for complete tissue and bone healing.[12,13] For example, WE43 alloy (part of a promising candidate alloy series for this type of application) has a typical corrosion rate of ∼0.7−1 mm/year.[14,15] Witte et al.[16] found that WE43 alloy completely degrades within 18 weeks in vivo. Electrons released from the dissolution of Mg (anodic reaction) are consumed by the cathodic reaction to generate H_2 gas.[17] The Mg^{2+} and OH^- ions formed in anodic and cathodic reactions could then combine to form $Mg(OH)_2$.[18] As indicated by the Pourbaix diagram, this corrosion product is normally unstable in the human body. Thus, Mg tends to corrode actively without protection in vivo. In addition, the low mechanical

Received: July 20, 2021
Accepted: October 14, 2021
Published: October 26, 2021

https://doi.org/10.1021/acsabm.1c00826
ACS Appl. Bio Mater. 2021, 4, 7903−7912

strength of Mg makes it susceptible to high wear rates, especially in a corrosive physiological environment.[19] The formation of extensive wear debris on bone screws and anchors could result in an undesirable inflammatory reaction and implant loosening due to osteolysis.[20] Therefore, it is critical to simultaneously enhance the surface corrosion and wear resistance, i.e., tribocorrosion resistance of Mg alloys, to enable their potential usage as degradable load-bearing implants.

Among various surface treatment techniques for metals, laser shock peening (LSP) has generated considerable interest lately as a noncontacting photon-modification method due to its high precision, simple operability, and excellent reliability and efficiency.[21,22] Compared to traditional contacting-type methods (e.g., surface mechanical attrition, burr grinding, mechanical shot peening), surfaces treated with LSP not only exhibit enhanced fatigue life and corrosion resistance but also reduced stress relaxation during thermal exposure due to lower amounts of cold work involved,[23−27] making it highly desirable for biomedical applications. By employing nanosecond (ns) pulsed lasers, a high-intensity laser beam is irradiated onto the metal surface at a short period (typically 10−100 ns) to produce a high-energy plasma, which subsequently generates high-pressure shock waves.[21] Peening effect occurs when the pressure exceeds the Hugoniot elastic limit of the targeted materials.[28,29] Several previous studies showed that enhanced surface hardness and corrosion resistance could be achieved in metals after ns-LSP treatment as results of surface microstructure refinement, phase transformation, and residual stress generation.[24,29,30] For example, Ge et al.[31,32] reported a 34.1% increase in ultimate tensile strength and an 85.4% decrease in the corrosion rate of AZ31B Mg alloys after ns-LSP treatment, mainly due to the formation of compressive residual stresses and a nanostructured subsurface layer.

While most work on LSP so far uses ns-lasers,[32−34] few have studied the shock peening effect of femtosecond (fs) lasers,[35] where laser pulses are delivered to the metal surface in an ultrashort amount of time (on the order of one quadrillionth of a second) at precisely defined positions. Compared with ns-LSP, fs-LSP is found to introduce higher surface hardness at lower energy input[36] and interact differently with the confinement medium and protective coating than ns-laser.[35] For instance, Lu et al.[37] found that the surface hardness of Mg−3Gd alloy is improved by 70% through fs-LSP with 430 μJ pulse energy, as compared to 45.1% using ns-LSP with 9 J pulse energy due to less thermally facilitated subsurface structure relaxation. Apart from the effective strength improvement, fs-LSP is also beneficial to corrosion resistance enhancement. Wang et al.[38] discovered that the fs-LSP surface treatment effectively impedes corrosion crack formation and pits growth on the NiTi shape memory alloy. In addition, the smaller surface roughness generated by fs-LSP than that by ns-LSP could further attenuate the dissolution rate between peaks and recesses of a rough surface.[39] In this work, we demonstrate that the usage of fs-LSP with the laser power on the order of 10^{-2} μJ is highly effective in enhancing the surface properties of biodegradable WE43 alloys by employing a confining medium and an absorbent layer. Specifically, the effects of fs-LSP processing conditions (e.g., power density, confinement, and absorption material) on the hardness, corrosion, and tribocorrosion resistance of WE43 alloys were measured in a stagnant blood blank buffered saline (BBBS) environment at body temperature. Material's characterization is combined with finite element simulations to reveal the underlying structural evolutions and residual stress generations during fs-LSP, which are responsible for the enhancement of the surface performance of WE43 alloys for biomedical implant applications.

2. MATERIALS AND METHODS

2.1. Sample Preparation and Characterization. All specimens were cut from extruded WE43 plates (Hunan High Broad New Material Co., Ltd., China) into dimensions of 2 × 2 × 0.6 cm^3. The chemical composition of the alloy in wt % is ∼1.54 zirconium (Zr), ∼3.51 yttrium (Y), ∼2.27 neodymium (Nd), ∼1.45 gadolinium (Gd), and balance Mg. The average grain size of the as-received WE43 is 21.9 ± 7.1 μm, determined from the line-intercept method from the scanning electron microscope (SEM) images of etched surfaces (see the Supporting Information, Figure S1). Before fs-LSP, each sample was ground with abrasive SiC papers with sizes down to 1200 grit, polished using alcohol-based diamond polish suspension (Allied High-Tech Products Inc., California) from 3 to 0.25 μm, ultrasonically cleaned in ethanol for 10 min, and finally dried in air. The microstructure characteristics were performed by X-ray diffraction (XRD, Bruker D8 Discovery) on the samples before and after fs-LSP, at 40 kV and 40 mA with Cu Kα radiation and a 1 mm slit. A scan speed of 0.2° s/step with a step increment of 0.02 and 0.003° was applied for the large and small θ range scans, respectively. An atomic force microscope (AFM, Bruker) was employed to evaluate the surface roughness over areas of ∼20 × 20 μm^2. Hardness was measured using a Vickers hardness tester (LECO LV 700AT) with a load of 1000 gf and a dwell time of 10 s from at least seven separate tests on each sample. The surface morphology and composition were measured by a field-emission scanning electron microscope (FE-SEM, LEO 1550) equipped with an Oxford INCASynergy energy-dispersive X-ray spectroscopy (EDS) system. Transmission electron microscopy (TEM) was performed for selected samples using a JEOL JEM-2100 operated at 200 kV. Samples for TEM measurements were prepared via the standard lift-out method using a focused ion beam microscope (FIB, Helios600) after e-beam deposition of ∼200 nm and ion beam deposition of ∼3 μm Pt protective coating on the sample surface to minimize FIB-inducted damage and Ga contamination.

2.2. fs-LSP Experiment. The fs-LSP surface treatments of WE43 samples were conducted by a Ti:Sapphire laser (Spectra-Physics Mai Tai, VF-T1S laser) delivering femtosecond pulses with <60 fs pulse duration, at 750 nm wavelength and 80 MHz repetition rate, using a setup shown in Figure 1. The output power of the femtosecond laser was adjusted to 0.6 W for all treatments. The power density (I, GW/cm^2) was controlled by the spot size and the pulse energy of the laser beam using lenses with different focal lengths, i.e., f = 50 and 25 mm, and estimated as: $I = \frac{4E}{\pi \cdot \Delta t \cdot D^2}$, where E is the pulse energy per single

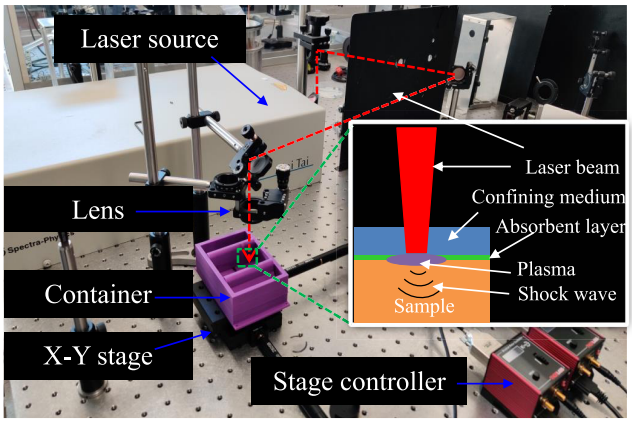

Figure 1. fs-LSP experimental setup. The inset image shows the schematic of a laser−sample interaction at the presence of a confining medium and an absorbent layer.

https://doi.org/10.1021/acsabm.1c00826
ACS Appl. Bio Mater. 2021, 4, 7903−7912

pulse, Δt is the pulse duration, and D is the diameter of the laser spot size. The samples were scanned at 0.5 mm/s in a zigzag pattern using a custom-made motorized x−y stage (Thorlabs, PT1-Z8). To obtain a homogeneous power density on the samples, 50% overlap between adjacent laser spots was used for all samples. Table 1 summarizes all

Table 1. Summary of Femtosecond Laser Shock Peening Processing Parameters

sample group ID	focal length (mm)	spot size (ϕ mm)	power density (GW/cm^2)	absorbent layer	confining medium
fs-LSP-air-7	50	∼0.05	7	NA	NA
fs-LSP-water-7	50	∼0.05	7	NA	water
fs-LSP-water-tape-7	50	∼0.05	7	black tape	water
fs-LSP-quartz-tape-7	50	∼0.05	7	black tape	quartz
fs-LSP-quartz-tape-28	25	∼0.02	28	black tape	quartz

samples tested under various processing parameters. For direct ablated samples (fs-LSP-air-7), the samples were directly treated by the laser in air without an absorbent layer or a confining medium. For other samples, deionized water (∼3 mm thickness) or quartz (∼2 mm thickness) were employed as a confining medium, while vinyl electrical black tape (3M-700) with ∼0.177 mm thickness was used as an adsorbent layer.

2.3. Corrosion and Tribocorrosion Tests. To evaluate the effect of fs-LSP on a metal surface, all electrochemical measurements were performed in the BBBS solution with pH of 7.0−7.2 at 37.01 ± 0.43 °C using a Gamry Reference 600 potentiostat/galvanostat/ZRA in the three-electrode configuration, where the specimen, activated titanium mesh, and a commercial silver−silver chloride electrode (1 M KCl internal solution) served as the working (WE), counter (CE), and reference (RE) electrodes, respectively. Potentiodynamic polarization (PD) tests were carried out on all specimens with an effective exposed area of ∼0.5 cm^2. After stabilization at the open circuit potential (OCP) for ∼5 min, the PD tests started from −0.2 V below OCP and terminated at 0.5 V above OCP under a constant scan rate of 1 mV/s. Electrochemical impedance spectroscopy (EIS) tests were conducted by applying a 10 mV root mean square of AC voltage under OCP from 100 mHz to 100 kHz with five points per decade in the BBBS solution, after 5 min of equilibrium time at OCP. All electrochemical results were collected and fitted using the Gamry E-chem software.

Tribocorrosion tests were performed using a multifunctional tribometer (MFT-5000, Rtec Instruments, California) with a built-in electrochemical cell in the three-electrode setup in the BBBS solution with the same pH, temperature, and WE exposed area as the corrosion tests. After ∼5 min of OCP stabilization, tribocorrosion tests were started by applying a 0.5 N normal load at 0.1 mm/s sliding velocity for 2 min over a 3 mm stroke length. An alumina ball (Al_2O_3, 4 mm diameter) was selected as the counterpart, and a new surface was used after each test to minimize contamination. A Dektak XT profilometer was used to measure the depth profile of wear tracks after the tribocorrosion tests. To ensure repeatability of results, all electrochemical and tribocorrosion tests were carried out at least three times for each sample group.

3. RESULTS AND DISCUSSION

3.1. Surface Morphology. To examine changes in the surface morphology of samples under the fs-LSP process, electron microscopes have been used. Figure 2 shows the SEM surface morphology of WE43 samples before and after fs-LSP treatments. There is no obvious difference between the surfaces of untreated and fs-LSP-air-7 samples (Figure 2a,b), indicating that under direct ablation in air, the low laser energy was not adequate to stimulate electrons so that little ionization or plasma was generated. On the other hand, for fs-LSP-water-7 samples treated under confined ablation in water without an absorbent layer (Figure 2c), except occasional dimple formation,[40] the surface is dominated by the formation of circular corrosion product (most likely $Mg(OH)_2$-rich hydroxide)[41] with ∼20−30 μm diameter as a result of Mg corrosion in water. When a black tape was used as an absorbent layer, more dramatic surface morphological changes were observed. For sample fs-LSP-water-tape-7, Figure 2d shows the formation of extensive craters on the surface, indicating that the energy absorption was significantly improved by the black tape to induce laser ablation. A similar treatment using an aluminum tape (results not shown here), however, leads to a negligible surface morphological change due to its higher surface reflectivity or lower (80%) laser energy absorption than that of black tape (100%). It was also observed that when either static or flowing water was used as the confining medium, H_2 gas bubbles frequently occur on the sample surfaces due to metal corrosion,[42] greatly impeding uniform laser peening effect. Thus, the usage of water as a confining medium should be avoided for actively corroding metals such as Mg alloys. When quartz was used as the confining medium, fewer craters and more ripplelike structures and surface nodules were seen on the sample surface, as shown in Figure 2e. Under a higher laser power density of 28 GW/cm^2, the sample surface shows uniform ripple, a.k.a. laser induced the formation of periodic surface structures[43] over the

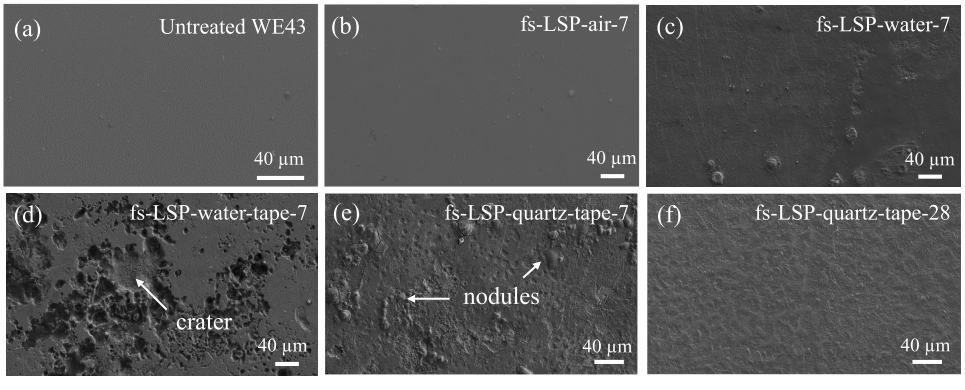

Figure 2. SEM surface morphology of (a) untreated and (b−f) fs-LSP-treated WE43 Mg samples under different conditions as listed in Table 1.

https://doi.org/10.1021/acsabm.1c00826
ACS Appl. Bio Mater. 2021, 4, 7903−7912

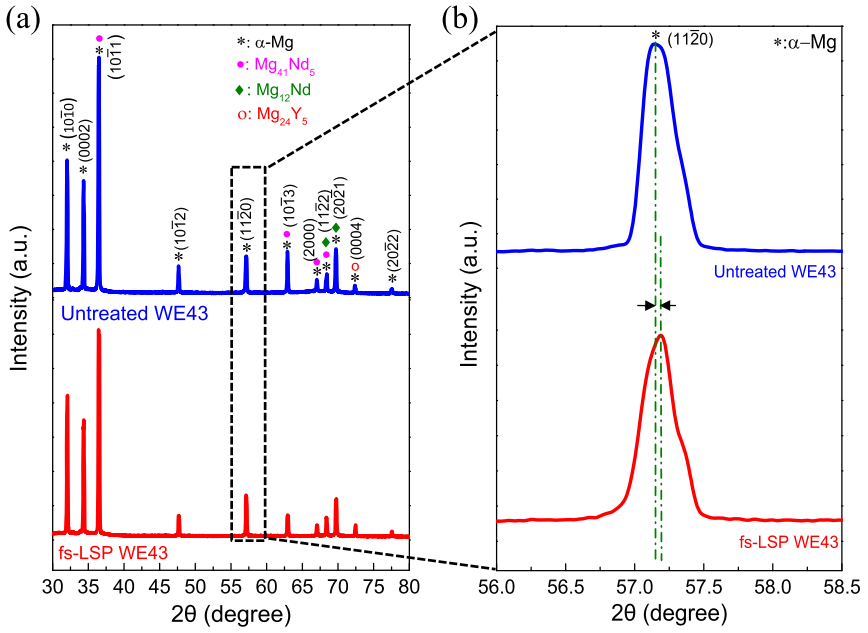

Figure 3. XRD (a) 2θ spectra and (b) zoomed-in spectra of the box area (a) of untreated and fs-LSP-treated WE43 Mg alloy. The fs-LSP treatment of WE43 was performed using quartz as a confining medium and a black tape as an absorbent layer at 28 GW/cm^2 power density.

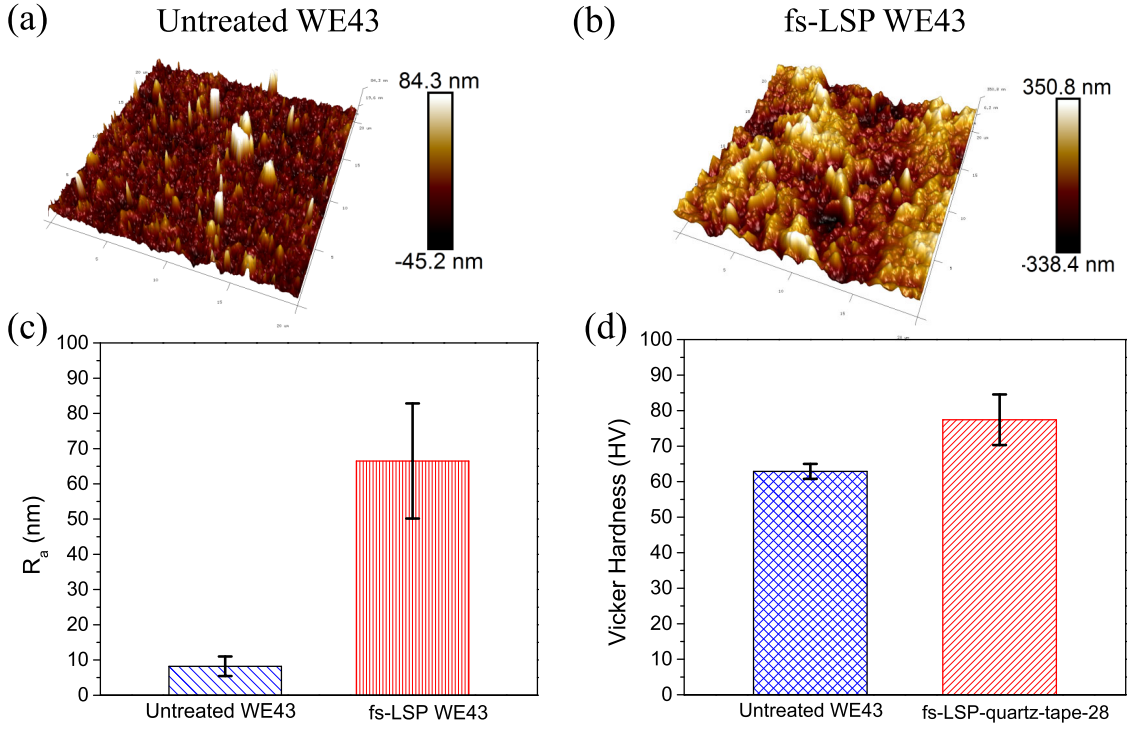

Figure 4. AFM images of WE43 Mg alloys (a) before and (b) after fs-LSP treatment, (c) surface roughness, and (d) micro-Vickers hardness of WE43 Mg samples with and without fs-LSP treatment using quartz as a confining medium and a black tape as an absorbent layer at 28 GW/cm^2 power density.

entire surface (Figure 2f). During the laser−sample interaction, surface electrons are energized by the laser energy, with a higher possibility to escape as irradiative energy increases. Such an ionization process produces plasma. If the power of the laser is appropriate, the expansion of such plasma leads to plastic deformation and ripple formation instead of surface ablation due to evaporation, plume and cone formation, as seen in the fs-LSP-water-tape-7 sample.[44−47] Comparing surface morphologies of all samples in Figure 2 shows that the fs-LSP-quartz-tape-28 samples are exhibited the most uniform formation of ripples. Hence, they were selected for the subsequent mechanical, corrosion, and tribocorrosion studies in Sections 3.2−3.4, and abbreviated as fs-LSP WE43 for simplicity hereafter.

3.2. Structure, Surface Morphology, and Mechanical Properties. The crystal structure of the untreated and fs-LSP WE43 samples was characterized by XRD and AFM. Both samples exhibited polycrystalline characteristics with an α-Mg

https://doi.org/10.1021/acsabm.1c00826
ACS Appl. Bio Mater. 2021, 4, 7903−7912

matrix and $Mg_{41}Nd_5$, $Mg_{24}Y_5$, and $Mg_{12}Nd$ precipitates, and no new phase was generated after the fs-LSP treatment, as shown in Figure 3. The diffraction peak of Mg $(11\bar{2}0)$ phase shifted slightly (~0.048°) toward the higher angle direction after fs-LSP, as compared to the untreated WE43 (indicated by arrows in Figure 3b), which could be related to the formation of lattice strain at the surface.[48] In addition, the full width at half-maximum (FWHM) of this diffraction peak exhibited a slight broadening (~0.271°) for the fs-LSP sample than that (~0.261°) of the untreated WE43, which is typically caused by grain refinement, or generation of high dislocation density and residual stress at the surface.[49,50] The AFM surface topography of the samples is presented in Figure 4a,b and the corresponding surface roughness (R_a) in Figure 4c. It can be seen that R_a increased after fs-LSP treatment due to the formation of ripples. Figure 4d shows the surface hardness of the WE43 sample increased by 23.1% after fs-LSP treatment.

To reveal the subsurface microstructure evolution after fs-LSP, the cross-section of fs-LSP-quartz-tape-28 samples was characterized by TEM and selected area electron diffraction (SAED) at various depths below the surface (Figure 5). It can

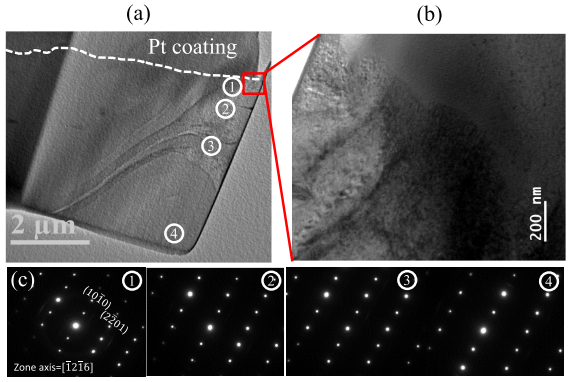

Figure 5. (a, b) Bright-field TEM image and (c) selected area electron diffractions of the fs-LSP WE43 sample at various depths below the surface as marked in (a).

be seen that the amount of plastic deformation at the surface has not resulted in significant grain refinement; instead, a higher dislocation density was present within the top ~1 μm below the surface (see additional information in Figure S2). In addition, the rotation of SAED patterns at various depths below the surface indicates the presence of a strain gradient, hence the formation of geometrically necessary dislocations after fs-LSP. It should be noted that, for thin FIB lamellar, the TEM sample lift-out procedure would relieve most of (if any) out-of-plane strain inevitably. Nevertheless, the deformation induced by a Gaussian laser beam is radial symmetric on the WE43 surface; hence, stress/strain measured from a 2D cross-sectional plane (perpendicular to the surface) is enough to determine that in 3D based on symmetry operation. In addition, fs-LSP involves a surface deformation with an affected depth significantly less than the grain size (~22 μm). Due to the presence of a strain gradient within the grain, the in-plane strain can be captured by accounting for the lattice rotation[51] from the undeformed (i.e., areas far away from the surface) and the deformed configurations (i.e., areas right below the surface), similar to that observed during severe adhesive wear.[52] Specifically, comparing the SAED patterns from locations 1 and 4 indicate a total rotation of ~0.5°, with the rotation axis perpendicular to the image plane, corresponding to a residual strain of ~0.5% (more details are provided in Figure S3). However, such interpretation of strain should be cautioned, as the bend contour (equal inclination fringe) in Figure 5a indicates the presence of local curvature, which may also affect the appearance of the SAED patterns. Combined with the FE simulation results shown in the Supporting Information, it is concluded here that the residual elastic strain, if any, is insignificant in WE43 after fs-LSP.

3.3. Corrosion Behavior. An improvement of the corrosion behavior of the Mg alloy has been obtained with fs-LSP. Figure 6a presents typical PD results of untreated and fs-LSP WE43 samples under the BBBS solution at body temperature. It can be seen that the fs-LSP WE43 samples exhibited a shift toward positive of the corrosion potential (E_{corr}) and a reduction of corrosion current density (i_{corr}) than those of the untreated WE43 sample, indicating an enhancement of corrosion resistance due to reduced cathodic and anodic kinetics. Figure 6b,c shows their corresponding morphologies of corroded surfaces. The formation of the corrosion product of the untreated WE43 was found to be localized, while that of the fs-LSP samples was more uniform. In both cases, dehydration cracks were observed on the corrosion product, most likely due to the evaporation of water from magnesium hydroxide on the surface.[41] Table 2 summarizes the surface composition before and after corrosion for both samples from EDS analysis. It can be seen that after corrosion, a higher oxygen content was observed on the fs-LSP sample than the untreated sample, consistent with their more uniform distribution of the corrosion product on the surface.

To further understand their corrosion kinetics, EIS analysis was performed at OCP for both samples, and the results are shown in Figure 7. An equivalent circuit model[53] shown in Figure 7a was used to fit the experimental data, where R_s is the

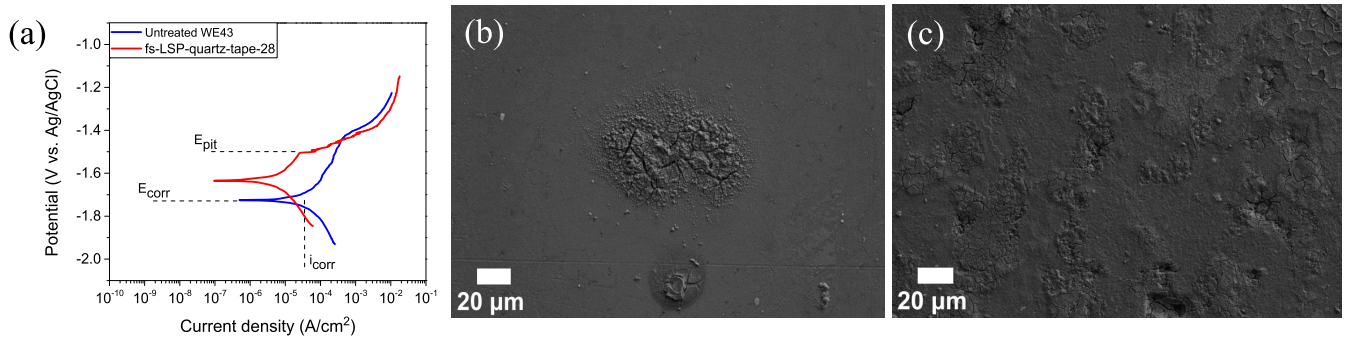

Figure 6. (a) Typical PD curves and post PD test surface morphologies of (b) untreated and (c) fs-LSP WE43 Mg samples.

https://doi.org/10.1021/acsabm.1c00826
ACS Appl. Bio Mater. 2021, 4, 7903−7912

Table 2. Summary of Surface Compositions (Measured by EDS Analysis) of Untreated and fs-LSP-Treated Samples before and after Corrosion

	untreated WE43		fs-LSP-quartz-tape-28	
elements (at %)	before corrosion	after corrosion	before corrosion	after corrosion
O	2.81 ± 0.2	22.8 ± 1.1	17.79 ± 1.2	30.3 ± 5.8
Mg	95.33 ± 0.3	75.1 ± 1.3	80.74 ± 1.1	67.87 ± 5.6
Y	1.21 ± 0.007	1.02 ± 0.01	0.95 ± 0.06	0.91 ± 0.06
Zr	0.15 ± 0.08	0.62 ± 0.07	0.13 ± 0.06	0.53 ± 0.04
Nd	0.38 ± 0.007	0.29 ± 0.01	0.3 ± 0.01	0.3 ± 0.01
Gd	0.14 ± 0.03	0.14 ± 0.01	0.11 ± 0.01	0.09 ± 0.03

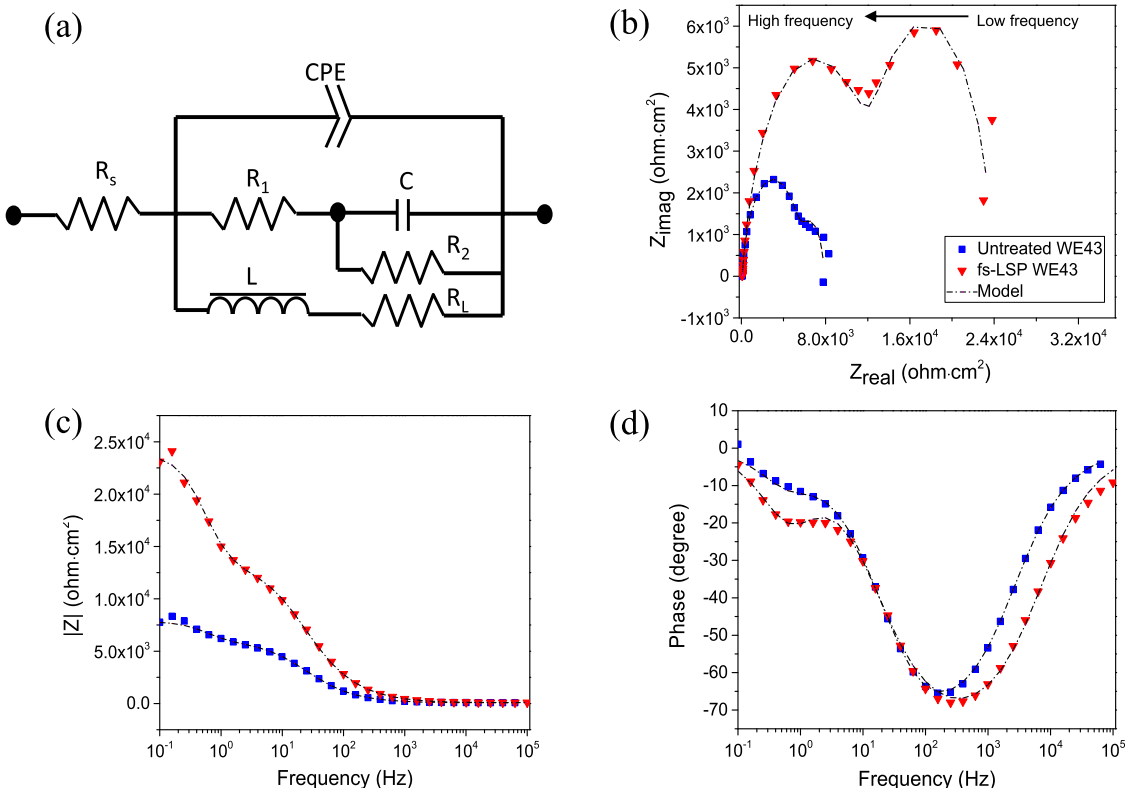

Figure 7. EIS results of WE43 Mg alloys with and without fs-LSP treatments: (a) equivalent circuit model used for the model fitting and (b) Nyquist plots and model fit. Bode plots of the (c) impedance magnitude, |Z|, and (d) phase shift are presented as a function of frequency.

Table 3. Summary of Equivalent Circuit Model Fitting Parameters Defined in Figure 7a

sample ID	R_s (Ω cm^2)	Y_{01} (cm^{-2} s^{-n} Ω^{-1})	a_1	CPE (F cm^{-2} s^{n-1})	R_1 (Ω cm^2)	C (F cm^{-2})	R_2 (Ω cm^2)	L (H)	R_L (Ω cm^2)
untreated WF43	76.9	3.79×10^{-6}	0.84	1.98×10^{-6}	8.83×10^{3}	7.31×10^{-5}	3.28×10^{3}	48.49	1.85×10^{4}
fs-LSP-quartz-tape-28	84.69	1.6×10^{-6}	0.834	7.75×10^{-7}	1.64×10^{4}	2.09×10^{-5}	1.81×10^{4}	55.32	7.62×10^{4}

resistance of the electrolyte between the working and the reference electrodes, R_1 is the resistance of the electrolyte through the corrosion products, R_2 is the charge-transfer resistance, C is the double-layer capacitance between the metal surface and electrolyte, and L and R_L are the inductance and the corresponding resistance of the inductor, respectively. In this model, CPE is the constant-phase element, representing nonideal capacitive behavior caused by surface inhomogeneity. Mathematically, CPE is defined as $Z = 1/Y \cdot (j\omega)^a$, where Y is a constant, j is the imaginary unit, ω is the angular frequency of the sinusoidal signal, and a is a coefficient between 0 and 1. All fitting parameters of the model are summarized in Table 3. Figure 7b shows typical the Nyquist plots and model fitting curves of both samples. Two capacitance loops can be found in the high- and low-frequency ranges, where the larger diameter of the semicircle of the fs-LSP sample indicates a higher charge-transfer resistance, hence better corrosion resistance than the untreated sample. Additionally, the inductive loop (where Z_{imag} is negative) was observed on the untreated WE43 sample, which likely formed after pitting induced accelerated anodic dissolution.[54] Note that such an inductive loop might disappear after a protective passive layer is generated, which is indeed observed in the fs-LSP sample. At high frequencies, the electrolyte resistance R_s was estimated to be ~77−85 Ω from Figure 7c. At lower frequencies, the polarization resistance of the fs-LSP sample was much higher than that of the untreated sample, in agreement with their PD behavior. In the phase-shift Bode plot, Figure 7d, the untreated WE43 sample exhibited a maximum phase angle close to 0° around 0.1 Hz, resembling the behavior from a simple Randles cell, indicating only one-

https://doi.org/10.1021/acsabm.1c00826
ACS Appl. Bio Mater. 2021, 4, 7903−7912

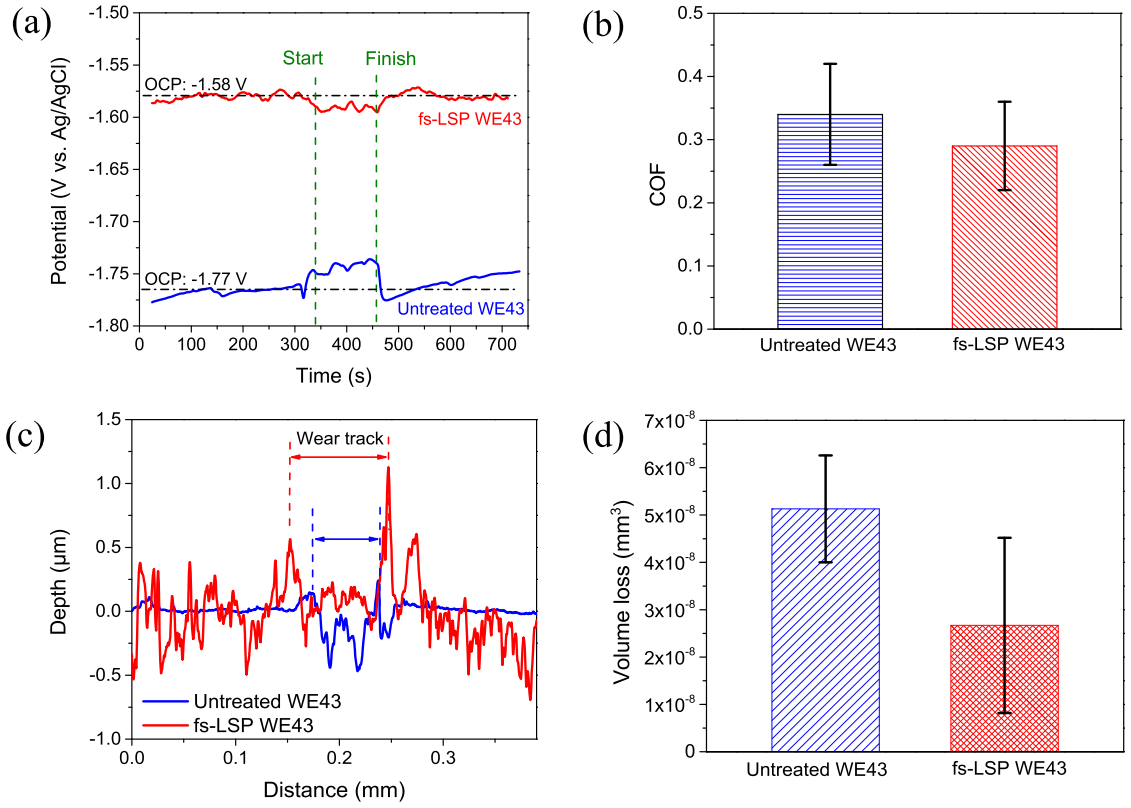

Figure 8. (a) Evolutions of OCP, (b) COF, (c) typical wear track depth profiles, and (d) the summary of volume loss of untreated and fs-LSP WE43 samples during tribocorrosion tests. The profiles in (c) were measured perpendicular to the sliding direction on the tribocorroded surface of all samples.

time constant was dominating, likely from the electrode/electrolyte double layer. On the other hand, the phase shift of the fs-LSP sample shows a small wave trough in the low-frequency region, characteristic of an electrical circuit with two relaxation processes,[55] where the additional relaxation process likely originated from the presence of an additional corrosion layer on the metal surface (i.e., electrode).

3.4. Tribocorrosion Results. The tribocorrosion results are summarized in Figures 8 and 9. Figure 8a shows the OCP evolution of both samples during tribocorrosion tests in the BBBS solution under body temperature. Before the onset of sliding, the stabilized OCP of fs-LSP samples was higher (nobler) than that of the untreated WE43 sample, which is consistent with their PD results (Figure 8a). As soon as the counter body sliding starts, the potential shifts toward the positive direction for the untreated WE43 sample, while a shift toward the more negative potential for the fs-LSP sample has been observed. Such different behavior can be understood as the following. For the untreated WE43 sample, the generated corrosion product layer was unprotected due to their discontinuity and defects.[56] The unworn area is thus actively corroded at a low corrosion potential. During tribocorrosion, the mechanical sliding imposes subsurface deformation within the wear track, similar to those imposed by LSP, hence leading to enhanced passivity and ennoblement of corrosion potential. On the other hand, the unworn surface of the fs-LSP sample was passivated due to laser peening, hence passivated during pure corrosion and exhibited a higher corrosion potential. Once scratched, the depassivation (i.e., mechanical removal of the passive film) on the wear track leads to the formation of more actively corroding surfaces, resulting in the potential

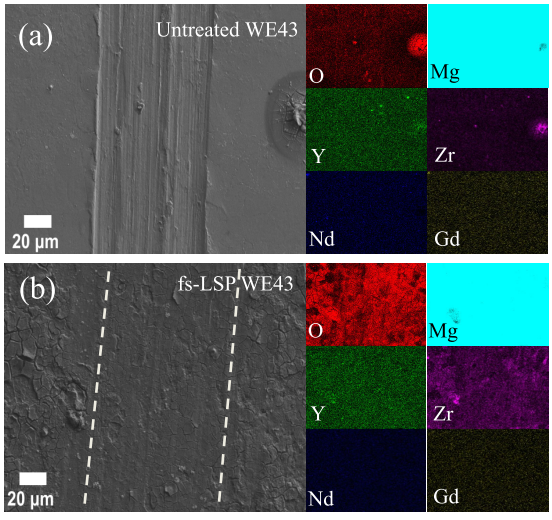

Figure 9. Surface SEM images after tribocorrosion tests of (a) untreated WE43 and (b) fs-LSP WE43 samples and corresponding EDS element mappings.

drop during sliding. When the test was over, the fs-LSP sample recovered its original OCP value, i.e., repassivated, with a small repassivation time of ~32 s, indicating a fast-repassivation kinetics. The average coefficient of friction (COF) during tribocorrosion is shown in Figure 8b. It can be seen that a slightly lower COF has been observed in the fs-LSP sample than that of the untreated counterpart, indicating that the corrosion product affected by the laser peening is also lubricious.

https://doi.org/10.1021/acsabm.1c00826
ACS Appl. Bio Mater. 2021, 4, 7903−7912

Figure 9 shows the post-tribocorrosion surface morphology and the corresponding EDS mappings. In Figure 9a, the wear track of the untreated WE43 sample exhibited deep grooves and pileups near the edge of the track, indicating the characteristics of abrasive wear. On the other hand, the wear track of the fs-LSP sample was much shallower and smoother (Figure 9b). In terms of element distribution, Mg, rare-earth elements, and oxygen are almost uniformly distributed on the surface of the untreated sample, with higher concentrations of O, Y, and Zr on the corrosion products. On the other hand, the O distribution of the fs-LSP sample was patchy, at a length scale similar to that of the surface ripples (~20−30 μm). The dimensions of wear tracks of both samples were evaluated and presented in Figure 8c, from which the total volume loss during tribocorrosion was calculated for both samples, as shown in Figure 8d. Approximately, 48% reduction in tribocorrosion rate was measured in the fs-LSP sample than that of the untreated one, indicating a significant enhancement of tribocorrosion resistance, in agreement with the enhancement of surface's mechanical and corrosion properties.

Finally, we briefly discuss the structural origin for the enhanced surface properties of WE43 after fs-LSP. While the improved surface hardness and corrosion resistance of Mg alloys through ns-LSP are typically attributed to grain refinement, generation of nanocrystalline layers, and beneficial residual stress,[57] our TEM analyses (Figure 5) indicate that there is no obvious grain refinement after fs-LSP. Hence, both surface hardening and corrosion resistance improvement in this work should be mainly attributed to the high dislocation density generated near the surface. On the one hand, the dense dislocation on the surface impedes dislocation motion, so the surface hardness is increased by strain hardening after fs-LSP, which further contributes to the shallow wear depth during tribocorrosion. On the other hand, the interception of dislocations at the surface is the preferred location for passive film growth according to the point-defect model.[58] It is believed that such high dislocation density considerably contributes to the rapid generation of a uniform and compact protective layer with high charge-transfer resistance on the fs-LSP sample surface during corrosion and also facilitates fast repassivation during tribocorrosion by modifying the surface activity. Another commonly observed structural modification during ns-LSP is the generation of residual stress. As shown in simulation results (Supporting Information, Figure S5), although present, both the affected depth and magnitude of residual stress are rather small during fs-LSP and hence are likely to play a less significant role than that of dislocations. Specifically, Figure S5a,b shows the simulated subsurface von Mises stress (σ_{vM}) and effective plastic strain (ε_{pl}) distribution during laser peening. The main deformation (see Figure S6 for stress components in different directions) is a compression stress in the surface-normal direction. A maximum effective plastic strain of 2.77% was observed during peening (Figure S5b), which became negligible (less than ~0.02%) once the laser was removed, leaving behind an elastic strain that was dominated by a compressive strain component of 0.49% in the surface with normal direction (Figure S7). It is noted that the simulated residual strain magnitude and residual stress depth (Figure S5d) are in great agreement with those measured experimentally from SAED analyses (Figures 5 and S3).

4. CONCLUSIONS

In this work, the effects of fs-LSP with ultralow pulse energy on the mechanical, corrosion, and tribocorrosion behavior of WE43 Mg alloys were investigated in a corrosive environment relevant to biomedical implant applications. It was found that surface morphology and the degree of peening effects strongly depend on the fs-LSP condition such as direct vs. confined ablation, with and without a confining medium and an absorbent layer. The optimum peening effect was found to occur in confined ablation conditions with the combination of a black tape and a quartz layer at 28 GW/cm^2. Comprehensive microstructure characterization indicates that fs-LSP leads to significant dislocation generation but no phase transformation or grain refinement below the surface. Such modified surface microstructure led to the enhancement of surface hardness, corrosion, and tribocorrosion resistance. The treated surface exhibits rapid-repassivation ability and high charge-transfer resistance, allowing the surface to quickly self-repair in a physiological environment once mechanically scratched. The coupling of advanced material characterization and FE simulation indicates that the generation of dislocations rather than residual stress contributes primarily to the remarkable enhancement of the surface performance of fs-LSP-treated WE43 Mg alloys.

■ ASSOCIATED CONTENT

Supporting Information

The Supporting Information is available free of charge at https://pubs.acs.org/doi/10.1021/acsabm.1c00826.

SEM of as-received WE43; TEM of fs-LSP-treated WE43; SAD pattern and misorientation angle measurements; and simulation results of residual stress (PDF)

■ AUTHOR INFORMATION

Corresponding Authors

Nguyen Q. Vinh − *Department of Physics and Center for Soft Matter and Biological Physics, Virginia Polytechnic Institute and State University, Blacksburg, Virginia 24061, United States*; Email: Vinh@vt.edu

Wenjun Cai − *Department of Materials Science and Engineering, Virginia Polytechnic Institute and State University, Blacksburg, Virginia 24061, United States*; orcid.org/0000-0002-9457-8705; Email: caiw@vt.edu

Authors

Wenbo Wang − *Department of Materials Science and Engineering, Virginia Polytechnic Institute and State University, Blacksburg, Virginia 24061, United States*; orcid.org/0000-0002-4111-1802

Chang-Yu Hung − *Department of Materials Science and Engineering, Virginia Polytechnic Institute and State University, Blacksburg, Virginia 24061, United States*

Leslie Howe − *Department of Physics and Center for Soft Matter and Biological Physics, Virginia Polytechnic Institute and State University, Blacksburg, Virginia 24061, United States*

Jia Chen − *Department of Materials Science and Engineering, Virginia Polytechnic Institute and State University, Blacksburg, Virginia 24061, United States*

Kaiwen Wang − *Department of Materials Science and Engineering, Virginia Polytechnic Institute and State University, Blacksburg, Virginia 24061, United States*

https://doi.org/10.1021/acsabm.1c00826
ACS Appl. Bio Mater. 2021, 4, 7903−7912

Vinh X. Ho − *Department of Physics and Center for Soft Matter and Biological Physics, Virginia Polytechnic Institute and State University, Blacksburg, Virginia 24061, United States;* orcid.org/0000-0001-5413-9030

Shannon Lenahan − *Department of Sustainable Biomaterials, Virginia Polytechnic Institute and State University, Blacksburg, Virginia 24061, United States*

Mitsuhiro Murayama − *Department of Materials Science and Engineering, Virginia Polytechnic Institute and State University, Blacksburg, Virginia 24061, United States;* orcid.org/0000-0003-1965-4891

Complete contact information is available at: https://pubs.acs.org/10.1021/acsabm.1c00826

Notes

The authors declare no competing financial interest.

■ ACKNOWLEDGMENTS

This research was financially supported by the U.S. National Science Foundation under Grant CMMI-1855651. The work was supported by the Air Force Office of Scientific Research under award number FA9550-18-1-0263. This study was partly supported by Nanoscale Characterization and Fabrication Laboratory (NCFL), Institute for Critical Technology and Applied Science (ICTAS), Virginia Tech and used shared facilities at the Virginia Tech National Center for Earth and Environmental Nanotechnology Infrastructure (NanoEarth), a member of the National Nanotechnology Coordinated Infrastructure (NNCI), supported by NSF (ECCS 1542100, ECCS 2025151). W.W. gratefully acknowledges Ya-Peng Yu (NCFL) for her assistance in FIB sample preparation.

■ REFERENCES

(1) Niinomi, M. Recent metallic materials for biomedical applications. *Metall. Mater. Trans. A* **2002**, *33*, 477−486.
(2) Hermawan, H.; Ramdan, D.; Djuansjah, J. R. Metals for Biomedical Applications. In *Biomedical Engineering - From Theory to Applications*; InTech, 2011; pp 411−430.
(3) Gepreel, M. A.-H.; Niinomi, M. Biocompatibility of Ti-alloys for long-term implantation. *J. Mech. Behav. Biomed. Mater.* **2013**, *20*, 407−415.
(4) Pietrzak, W. S.; Sarver, D.; Verstynen, M. Bioresorbable implants - Practical considerations. *Bone* **1996**, *19*, S109−S119.
(5) Nagels, J.; Stokdijk, M.; Rozing, P. M. Stress shielding and bone resorption in shoulder arthroplasty. *J. Shoulder Elb. Surg.* **2003**, *12*, 35−39.
(6) Milošev, I. Metallic materials for biomedical applications: Laboratory and clinical studies. *Pure Appl. Chem.* **2010**, *83*, 309−324.
(7) Zhen, Z.; Xi, T.-f.; Zheng, Y.-f. A review on in vitro corrosion performance test of biodegradable metallic materials. *Trans. Nonferrous Met. Soc. China* **2013**, *23*, 2283−2293.
(8) Prakasam, M.; Locs, J.; Salma-Ancane, K.; Loca, D.; Largeteau, A.; Berzina-Cimdina, L. Biodegradable materials and metallic implants—a review. *J. Funct. Biomater.* **2017**, *8*, No. 44.
(9) Staiger, M. P.; Pietak, A. M.; Huadmai, J.; Dias, G. Magnesium and its alloys as orthopedic biomaterials: a review. *Biomaterials* **2006**, *27*, 1728−1734.
(10) Marukawa, E.; Tamai, M.; Takahashi, Y.; Hatakeyama, I.; Sato, M.; Higuchi, Y.; Kakidachi, H.; Taniguchi, H.; Sakamoto, T.; Honda, J.; et al. Comparison of magnesium alloys and poly-l-lactide screws as degradable implants in a canine fracture model. *J. Biomed. Mater. Res., Part B* **2016**, *104*, 1282−1289.
(11) Rude, R. K.; Gruber, H. E. Magnesium deficiency and osteoporosis: animal and human observations. *J. Nutr. Biochem.* **2004**, *15*, 710−716.
(12) Virtanen, S. Biodegradable Mg and Mg alloys: Corrosion and biocompatibility. *Mater. Sci. Eng.: B* **2011**, *176*, 1600−1608.
(13) Atrens, A.; Liu, M.; Abidin, N. I. Z. Corrosion mechanism applicable to biodegradable magnesium implants. *Mater. Sci. Eng.: B* **2011**, *176*, 1609−1636.
(14) Gu, X. N.; Zhou, W. R.; Zheng, Y. F.; Cheng, Y.; Wei, S. C.; Zhong, S. P.; Xi, T. F.; Chen, L. J. Corrosion fatigue behaviors of two biomedical Mg alloys-AZ91D and WE43-In simulated body fluid. *Acta Biomater.* **2010**, *6*, 4605−4613.
(15) Jamesh, M.; Wu, G. S.; Zhao, Y.; Chu, P. K. Effects of silicon plasma ion implantation on electrochemical corrosion behavior of biodegradable Mg-Y-RE Alloy. *Corros. Sci.* **2013**, *69*, 158−163.
(16) Witte, F.; Kaese, V.; Haferkamp, H.; Switzer, E.; Meyer-Lindenberg, A.; Wirth, C. J.; Windhagen, H. In vivo corrosion of four magnesium alloys and the associated bone response. *Biomaterials* **2005**, *26*, 3557−3563.
(17) Frankel, G. S.; Samaniego, A.; Birbilis, N. Evolution of hydrogen at dissolving magnesium surfaces. *Corros. Sci.* **2013**, *70*, 104−111.
(18) Thomas, S.; Medhekar, N. V.; Frankel, G. S.; Birbilis, N. Corrosion mechanism and hydrogen evolution on Mg. *Curr. Opin. Solid State Mater. Sci.* **2015**, *19*, 85−94.
(19) Vignesh, R. V.; Padmanaban, R.; Govindaraju, M. Study on the corrosion and wear characteristics of magnesium alloy AZ91D in simulated body fluids. *Bull. Mater. Sci.* **2020**, *43*, No. 8.
(20) Jacobs, J. J.; Hallab, N. J.; Skipor, A. K.; Urban, R. M. Metal degradation products: a cause for concern in metal-metal bearings? *Clin. Orthop. Relat. Res.* **2003**, *417*, 139−147.
(21) Montross, C. S.; Wei, T.; Ye, L.; Clark, G.; Mai, Y.-W. Laser shock processing and its effects on microstructure and properties of metal alloys: a review. *Int. J. Fatigue* **2002**, *24*, 1021−1036.
(22) Fabbro, R.; Peyre, P.; Berthe, L.; Scherpereel, X. Physics and applications of laser-shock processing. *J. Laser Appl.* **1998**, *10*, 265−279.
(23) Lu, J.; Luo, K.; Zhang, Y.; Zhou, J.; Cui, X.; Zhang, L.; Zhong, J. Effects of laser shock processing and strain rate on tensile property of LY2 aluminum alloy. *Mater. Sci. Eng.: A* **2010**, *528*, 730−735.
(24) Lu, J.; Wu, L.; Sun, G.; Luo, K.; Zhang, Y.; Cai, J.; Cui, C.; Luo, X. Microstructural response and grain refinement mechanism of commercially pure titanium subjected to multiple laser shock peening impacts. *Acta Mater.* **2017**, *127*, 252−266.
(25) Zhang, R.; Zhou, X.; Gao, H.; Mankoci, S.; Liu, Y.; Sang, X.; Qin, H.; Hou, X.; Ren, Z.; Doll, G. L.; et al. The effects of laser shock peening on the mechanical properties and biomedical behavior of AZ31B magnesium alloy. *Surf. Coat. Technol.* **2018**, *339*, 48−56.
(26) Park, C.; Jung, D.; Chun, E.-J.; Ahn, S.; Jang, H.; Kim, Y.-J. Effect of laser shock peening without coating on fretting corrosion of copper contacts. *Appl. Surf. Sci.* **2020**, *514*, No. 145917.
(27) Lu, J.; Qi, H.; Luo, K.; Luo, M.; Cheng, X. Corrosion behaviour of AISI 304 stainless steel subjected to massive laser shock peening impacts with different pulse energies. *Corros. Sci.* **2014**, *80*, 53−59.
(28) Sundar, R.; Ganesh, P.; Gupta, R. K.; Ragvendra, G.; Pant, B.; Kain, V.; Ranganathan, K.; Kaul, R.; Bindra, K. Laser Shock Peening and its Applications: A Review. *Lasers Manuf. Mater. Process.* **2019**, *6*, 424−463.
(29) Gujba, A. K.; Medraj, M. Laser peening process and its impact on materials properties in comparison with shot peening and ultrasonic impact peening. *Materials* **2014**, *7*, 7925−7974.
(30) Mao, B.; Liao, Y.; Li, B. Gradient twinning microstructure generated by laser shock peening in an AZ31B magnesium alloy. *Appl. Surf. Sci.* **2018**, *457*, 342−351.
(31) Ge, M.-Z.; Xiang, J.-Y.; Yang, L.; Wang, J. Effect of laser shock peening on the stress corrosion cracking of AZ31B magnesium alloy in a simulated body fluid. *Surf. Coat. Technol.* **2017**, *310*, 157−165.
(32) Ge, M.-Z.; Xiang, J.-Y. Effect of laser shock peening on microstructure and fatigue crack growth rate of AZ31B magnesium alloy. *J. Alloys Compd.* **2016**, *680*, 544−552.

(33) Chin, K. S.; Idapalapati, S.; Ardi, D. T. Thermal stress relaxation in shot peened and laser peened nickel-based superalloy. *J. Mater. Sci. Technol.* **2020**, *59*, 100−106.
(34) Tong, J.; Dalby, S.; Byrne, J.; Henderson, M. B.; Hardy, M. C. Creep, fatigue and oxidation in crack growth in advanced nickel base superalloys. *Int. J. Fatigue* **2001**, *23*, 897−902.
(35) Li, Y. X.; Ren, Z. C.; Jia, X.; Yang, W. J.; Nassreddin, N.; Dong, Y. L.; Ye, C.; Fortunato, A.; Zhao, X. The effects of the confining medium and protective layer during femtosecond laser shock peening. *Manuf. Lett.* **2021**, *27*, 26−30.
(36) Lee, D.; Kannatey-Asibu, E., Jr. Experimental investigation of laser shock peening using femtosecond laser pulses. *J. Laser Appl.* **2011**, *23*, No. 022004.
(37) Lu, C.; Ge, L.; Zhu, B.; Li, Y.; Chen, X.; Zeng, X.; Chen, Y. Effective femtosecond laser shock peening on a Mg−3Gd alloy at low pulse energy 430 μJ of 1 kHz. *J. Magnesium Alloys* **2019**, *7*, 529−535.
(38) Wang, H.; Jürgensen, J.; Decker, P.; Hu, Z.; Yan, K.; Gurevich, E. L.; Ostendorf, A. Corrosion behavior of NiTi alloy subjected to femtosecond laser shock peening without protective coating in air environment. *Appl. Surf. Sci.* **2020**, *501*, No. 144338.
(39) Zhang, R. X.; Hou, X. N.; Zhou, X. F.; Gao, H. Y.; Mankoci, S.; Qin, H. F.; Ren, Z. C.; Doll, G. L.; Martini, A.; Dong, Y. L.; Sahai, N.; Ye, C. In *Effects of Laser Shock Peening on the Wear and Degradation Behaviors of Magnesium Alloys*, Proceedings of the ASME 11th International Manufacturing Science and Engineering Conference, 2016; Vol. *2*.
(40) Li, Y.; Ren, Z.; Jia, X.; Yang, W.; Nassreddin, N.; Dong, Y.; Ye, C.; Fortunato, A.; Zhao, X. The effects of the confining medium and protective layer during femtosecond laser shock peening. *Manuf. Lett.* **2021**, *27*, 26−30.
(41) Mraied, H.; Wang, W. B.; Cai, W. J. Influence of chemical heterogeneity and microstructure on the corrosion resistance of biodegradable WE43 magnesium alloys. *J. Mater. Chem. B* **2019**, *7*, 6399−6411.
(42) Elango, K.; Hoppius, J. S.; Kukreja, L. M.; Ostendorf, A.; Gurevich, E. L. Studies on ultra-short pulsed laser shock peening of stainless-steel in different confinement media. *Surf. Coat. Technol.* **2020**, *397*, No. 125988.
(43) Tull, B. R.; Carey, J. E.; Mazur, E.; McDonald, J. P.; Yalisove, S. M. Silicon surface morphologies after femtosecond laser irradiation. *MRS Bull.* **2006**, *31*, 626−633.
(44) Zhao, X.; Shin, Y. C. A two-dimensional comprehensive hydrodynamic model for femtosecond laser pulse interaction with metals. *J. Phys. D: Appl. Phys.* **2012**, *45*, No. 105201.
(45) Toyserkani, E.; Rasti, N. Ultrashort Pulsed Laser Surface Texturing. In *Laser Surface Engineering: Processes and Applications*; Elsevier, 2015; pp 441−453.
(46) Raillard, B.; Mücklich, F. Ablation Effects of Femtosecond Laser Functionalization on Surfaces. In *Laser Surface Engineering*; Elsevier, 2015; pp 565−581.
(47) Han, Y.; Qu, S. The ripples and nanoparticles on silicon irradiated by femtosecond laser. *Chem. Phys. Lett.* **2010**, *495*, 241−244.
(48) Zhang, S.; Xie, H.; Zeng, X.; Hing, P. Residual stress characterization of diamond-like carbon coatings by an X-ray diffraction method. *Surf. Coat. Technol.* **1999**, *122*, 219−224.
(49) Williamson, G.; Hall, W. X-ray line broadening from filed aluminium and wolfram. *Acta Metall.* **1953**, *1*, 22−31.
(50) Chen, X.; Li, Y.; Zhu, Y.; Yang, B. Enhanced irradiation and corrosion resistance of 316LN stainless steel with high densities of dislocations and twins. *J. Nucl. Mater.* **2019**, *517*, 234−240.
(51) Yu, H. B.; Liu, J. L.; Karamched, P.; Wilkinson, A. J.; Hofmann, F. Mapping the full lattice strain tensor of a single dislocation by high angular resolution transmission Kikuchi diffraction (HR-TKD). *Scr. Mater.* **2019**, *164*, 36−41.
(52) Cai, W.; Bellon, P.; Beaudoin, A. J. Probing the subsurface lattice rotation dynamics in bronze after sliding wear. *Scr. Mater.* **2019**, *172*, 6−11.
(53) Bland, L.; King, A.; Birbilis, N.; Scully, J. Assessing the corrosion of commercially pure magnesium and commercial AZ31B by electrochemical impedance, mass-loss, hydrogen collection, and inductively coupled plasma optical emission spectrometry solution analysis. *Corrosion* **2015**, *71*, 128−145.
(54) Feliu, S. Electrochemical impedance spectroscopy for the measurement of the corrosion rate of magnesium alloys: Brief review and challenges. *Metals* **2020**, *10*, No. 775.
(55) Chen, J.; Xiao, J. W.; Poplawsky, J.; Michel, F. M.; Deng, C.; Cai, W. J. The origin of passivity in aluminum-manganese solid solutions. *Corros. Sci.* **2020**, *173*, No. 108749.
(56) Mraied, H.; Wang, W.; Cai, W. Influence of chemical heterogeneity and microstructure on the corrosion resistance of biodegradable WE43 magnesium alloys. *J. Mater. Chem. B* **2019**, *7*, 6399−6411.
(57) Ren, X.; Huang, J.; Zhou, W.; Xu, S.; Liu, F. Surface nanocrystallization of AZ91D magnesium alloy induced by laser shock processing. *Mater. Des.* **2015**, *86*, 421−426.
(58) Gaberšček, M.; Pejovnik, S. Impedance spectroscopy as a technique for studying the spontaneous passivation of metals in electrolytes. *Electrochim. Acta* **1996**, *41*, 1137−1142.

https://doi.org/10.1021/acsabm.1c00826
ACS Appl. Bio Mater. 2021, 4, 7903−7912

Supporting Information

Enabling High-Performance Surfaces of Biodegrade Magnesium Alloys via Femtosecond Laser Shock Peening with Ultra-low Pulse Energy

Wenbo Wang[1], Chang-Yu Hung[1], Leslie Howe[2], Jia Chen[1], Kaiwen Wang[1], Vinh X. Ho[2], Shannon Lenahan[3], Mitsuhiro Murayama[1], Nguyen Q. Vinh[2,], Wenjun Cai[1,*]*

1. Department of Materials Science and Engineering, Virginia Polytechnic Institute and State University, Virginia 24061, United States

2. Department of Physics and Center for Soft Matter and Biological Physics, Virginia Polytechnic Institute and State University, Virginia 24061, United States

3. Department of Sustainable Biomaterials, Virginia Polytechnic Institute and State University, Virginia 24061, United States

* Corresponding authors E-mail addresses: Vinh@vt.edu (N.Q. Vinh), caiw@vt.edu (W. Cai).

1. Electron microscopy images

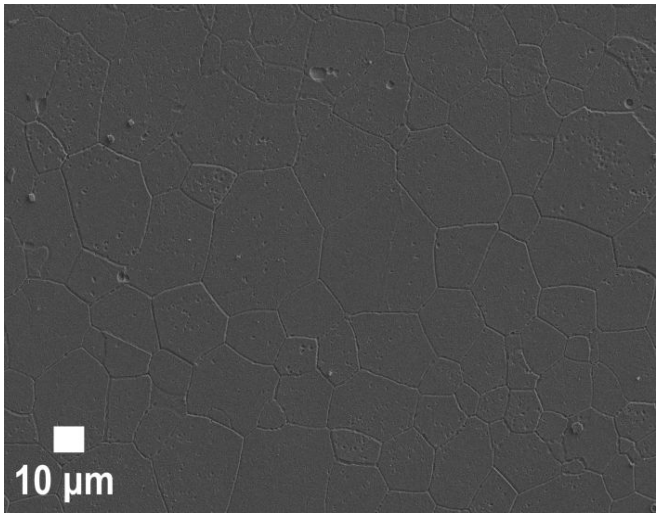

Figure S1. Surface SEM image of as-received WE43 after etching in a 1:5 (volume ratio) mixture of HNO_3 and C_2H_6O solutions for 40 seconds at room temperature.

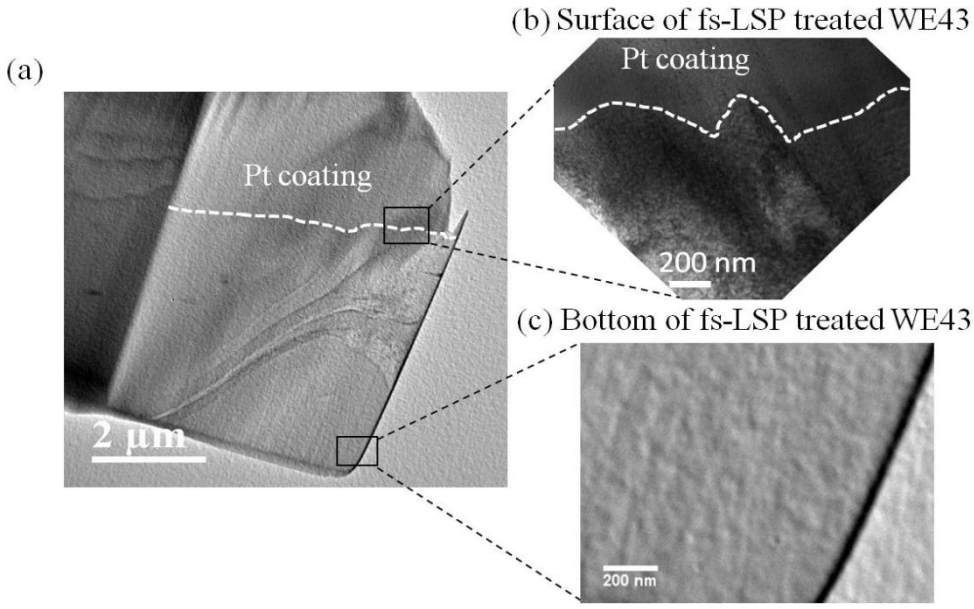

Figure S2. Bright field TEM image of fs-LSP WE43 sample. HRTEM images (b) and (c) are taken from box areas marked in (a).

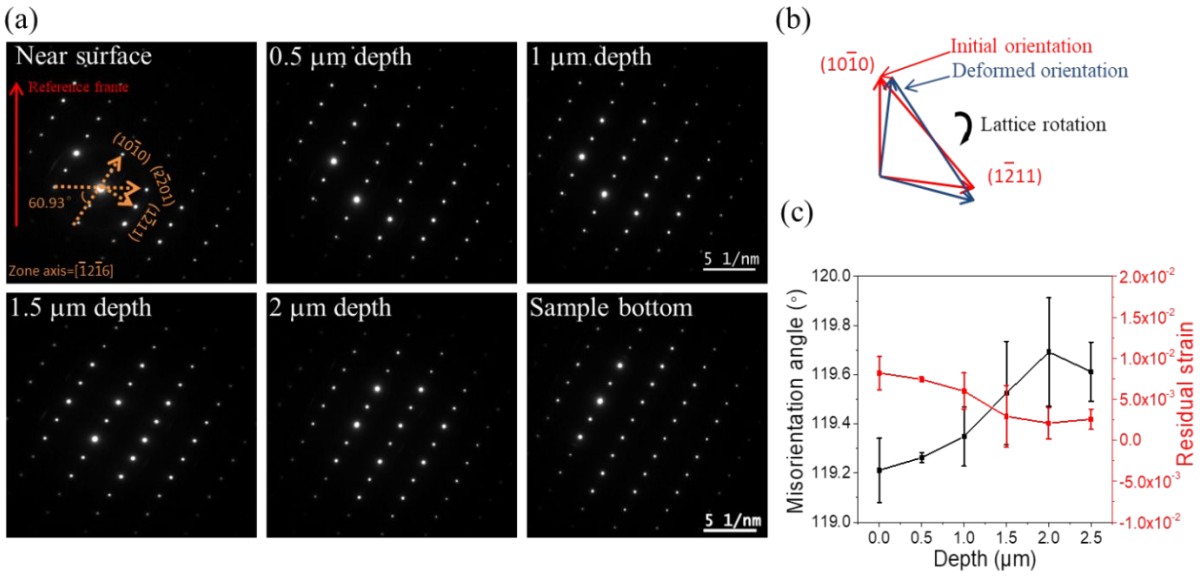

Figure S3. (a) SAED patterns of fs-LSP WE43 sample at various depths below the surface, (b) schematic representation of in-plane lattice rotation, and (c) the measured misorientation angle and calculated residual strain as a function of depth.

2. Finite element simulations

A two-dimensional (2D) axisymmetric finite element model was developed to simulate residual stress/strain generation from fs-LSP using the ABAQUS software, as shown schematically in Figure S4. The workpiece dimensions were set up as a square with 100 µm in both the *r*- and *z*-directions and a laser spot size of ~ 20 µm. The bottom and right sides were set as a fixed constraint with non-deformation boundary conditions. CAX4R (4-node bilinear axisymmetric quadrilateral, reduced integration and hourglass control) mesh elements were selected for finite computational domain, and the mesh

size was refined from 1.0 to 0.5 μm toward the center of laser beam in both *r*- and *z*-directions after convergence analysis. The peak pressure (P) generated from the shock wave was estimated by Fabbro's model as[1]: $P(\mathrm{GPa}) = 0.01\sqrt{\frac{\alpha}{2\alpha+3}} \cdot \sqrt{Z} \cdot \sqrt{I}$, where I is the power density (GW/cm^2), Z is the reduced shock impedance (g·cm^{-2}·s^{-1}) between the confining material and the workpiece, and α is the efficiency of the interaction (α = 0.1 – 0.2). It should be noted that Fabbro's model is generally used in ns-LSP. In current simulation, the early stage of interaction between laser and target, i.e., two-temperature model, is not considered. Thus, the peak pressure of fs-LSP was estimated by Fabbro's model for simplicity.[2] Due to the ultrashort pulse duration, a linear triangle ramping pressure was utilized on the top surface, as shown in Figure S4 inset, instead of the conventional Gaussian temporal profile, and total loading time was adjusted to twice the pulse duration (Δt).[3] The stable time increment during ABAQUS/Explicit analysis is smaller than the stress stabilization time in order to avoid numerical instability and obtain accurate results.[4] The Johnson-Cook model was used to simulate the rate-dependent mechanical behavior of WE43, as described by the flow stress, $\sigma = \left(A + B\varepsilon^n\right) \cdot \left(1 + C\ln\left(\dot{\varepsilon}/\dot{\varepsilon_0}\right)\right) \cdot \left(1 - T^m\right)$, where A is the yield stress, B is work hardening modulus, C is the strain rate sensitivity, n is the work hardening coefficient, ε is the strain, $\dot{\varepsilon}$ is the strain rate, T is the dimensionless temperature, and m is the thermal soften coefficient. The materials parameters used in the present work are estimated from Ref. [5] and information from the vendor.

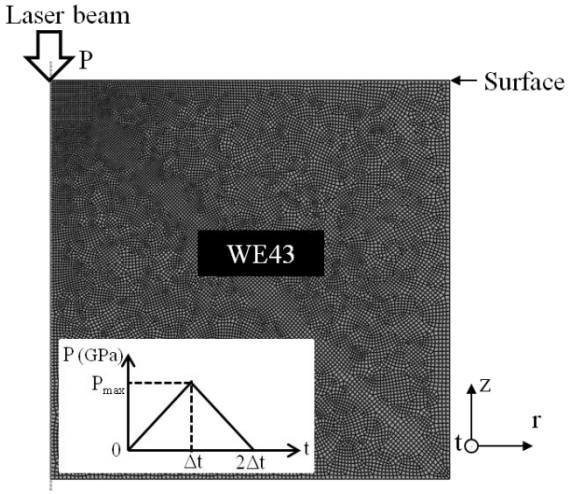

Figure S4. FE model geometry setup and meshing, where r, z, t in the coordinate system represents the radial, normal, and transverse direction, respectively. Inset graph shows the imposed laser pressure temporal profile used in the simulation.

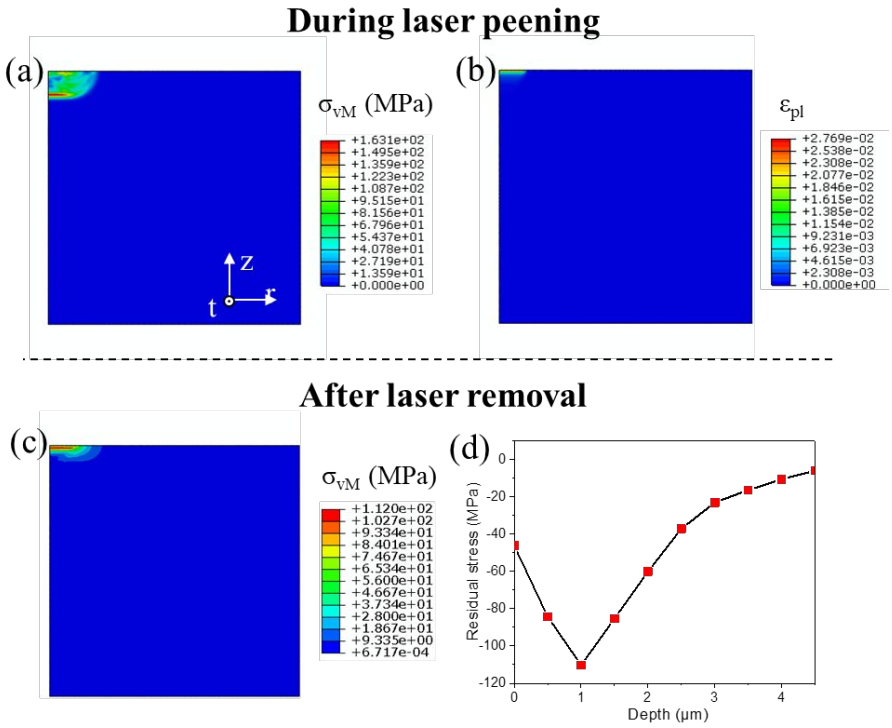

Figure S5. FE simulated results of (a) von Mises stress and (b) effective plastic strain during laser peening. FE simulated (c) von Mises stress and (d) maximum residual

stress depth profile after laser removal on WE43 surface after fs-LSP treatment using pressure profile defined in Figure S4 inset.

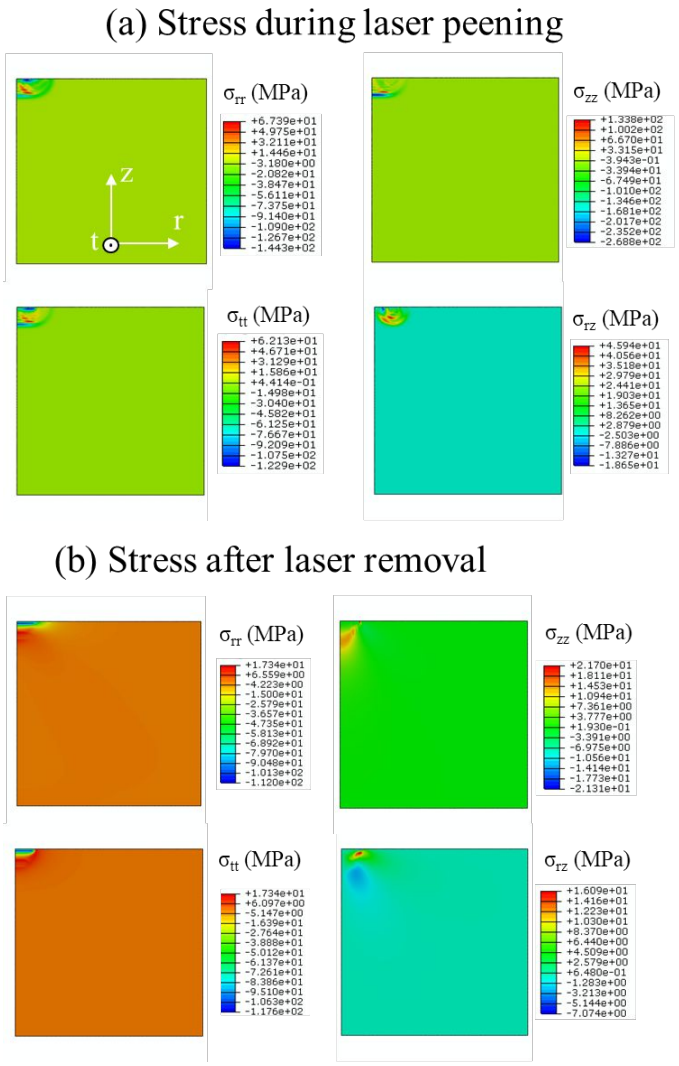

Figure S6. FE simulated results of 2D stress components (a) during laser peening and (b) after laser removal using coordinate system defined in (a).

(a) Strain during laser peening

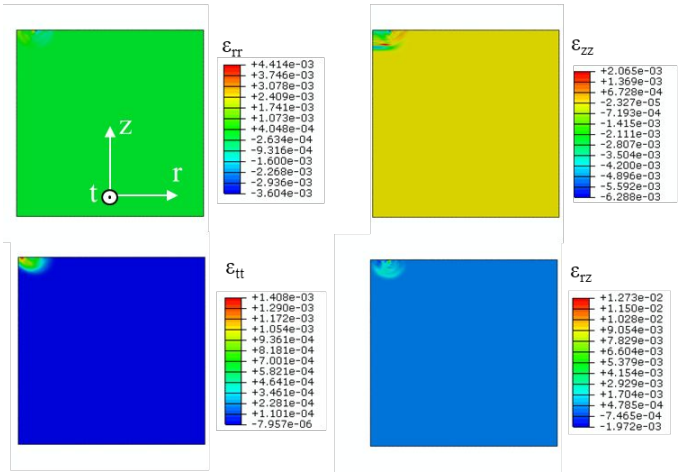

(b) Strain after laser removal

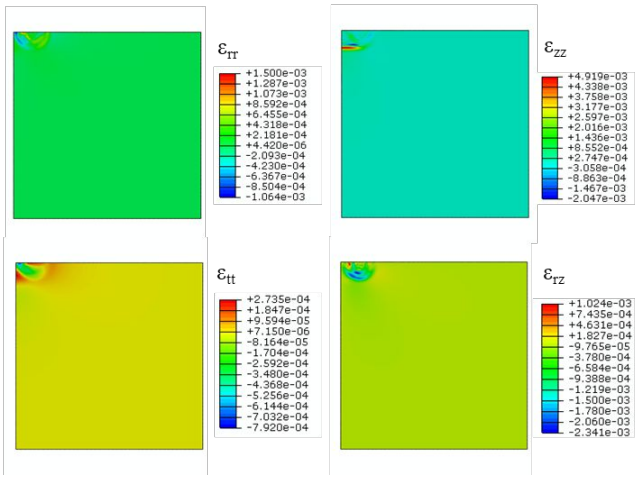

Figure S7. FE simulated results of 2D logarithmic strain components (a) during laser peening and (b) after laser removal using coordinate system defined in (a).

References:

1. Fabbro, R.; Fournier, J.; Ballard, P.; Devaux, D.; Virmont, J., Physical study of laser‐produced plasma in confined geometry. *Journal of applied physics* **1990,** *68* (2), 775-784.

2. Ye, Y.; Feng, Y.; Lian, Z.; Hua, Y., Plastic deformation mechanism of polycrystalline copper foil shocked with femtosecond laser. *Applied surface science* **2014,** *309*, 240-249.

3. Stein, P.; García, O.; Morales, M.; Huber, H.; Molpeceres, C., Numerical simulation of laser ablation for photovoltaic materials. *Applied surface science* **2012,** *258* (23), 9288-9291.

4. Kim, J. H.; Kim, Y. J.; Kim, J. S., Effects of simulation parameters on residual stresses for laser shock peening finite element analysis. *Journal of Mechanical Science Technology* **2013,** *27* (7), 2025-2034.

5. Platts, A. T., *Understanding and Simulating High Strain Rate Deformation of Magnesium WE43 Plate Products*. The University of Manchester (United Kingdom): 2019.